ORIGINAL PAPER

Role of Mn^{2+} Doping on Structural, Morphological, and Opto-Magnetic Properties of Spinel $Mn_xCo_{1-x}Fe_2O_4$ ($x = 0.0, 0.1, 0.2, 0.3, 0.4,$ and 0.5) Nanocatalysts

A. Manikandan · M. Durka · S. Arul Antony

Abstract Spinel $Mn_xCo_{1-x}Fe_2O_4$; $x = 0.0, 0.1, 0.2, 0.3, 0.4,$ and 0.5) nanoparticles were synthesized by urea-assisted auto combustion method using nitrates of Co, Mn and Fe as the starting materials and urea as the fuel. X-ray diffraction (XRD) analysis showed that all composition was found to have a cubic spinel structure. The average crystallite size of the samples was estimated using the Debye-Scherrer formula and was found to be in the range of 22.62 and 36.45 nm. The lattice parameter increased from 8.432 to 8.457 Å with increasing the Mn^{2+} content, which was determined by Rietveld analysis. High-resolution scanning electron microscopy (HR-SEM) and high-resolution transmission electron microscopy (HR-TEM) analyses were used to study the morphological variation, and the results showed a nanosized particle-like morphology. Energy-dispersive X-ray (EDX) results showed that the composition of the elements was relevant as expected from the synthesis. The bandgap energy of the pure $CoFe_2O_4$ was estimated to be 2.33 eV from UV-visible diffuse reflectance spectroscopy (DRS). With the increase of Mn^{2+} ion, the bandgap energy increased from 2.35 to 2.42 eV. The magnetic properties of the samples were investigated at room temperature by using a vibrating sample magnetometer (VSM). The magnetic hysteresis (M-H) loop confirmed the superparamagnetic nature of pure $CoFe_2O_4$ and a weak ferromagnetic behavior of Mn^{2+} doped $CoFe_2O_4$ samples with specific saturation magnetization in the range of 55.16 ± 24 and 66.92 ± 05 emu/g. All compositions of spinel $Mn_xCo_{1-x}Fe_2O_4$ samples were successfully tested as catalyst for the conversion of benzyl alcohol, which has resulted in 62.75 and 92.62 % conversion efficiency of $CoFe_2O_4$ and $Mn_{0.5}Co_{0.5}Fe_2O_4$, respectively.

1 Introduction

Recently, nanocrystalline spinel ferrites have been broadly developed for both fundamental scientific interest and technological applications including information storage, electronic devices, biomedical and catalysts [1–5] Spinel ferrites, with a general formula $M^{2+}(Fe^{3+})_2O_4$ ($M^{2+} = Mn^{2+}, Co^{2+}, Cu^{2+}, Ni^{2+},$ etc.) have been the most exciting magnetic materials, where M^{2+} and Fe^{3+} ions can occupy either tetrahedral (A–) or octahedral (B–) sites and oxygen has a fcc close packing arrangement. Among the spinel ferrites, cobalt ferrite ($CoFe_2O_4$) is an important and well-known hard magnetic material. Recently, $CoFe_2O_4$ has received great attention in the area of catalysts, magnetic storage devices, microwave and electronic devices, due to the high coercivity values (H_c, 5400 Oe), high chemical stability, good electrical insulation, significant mechanical hardness, as well as moderate saturation magnetization

A. Manikandan (✉) · S. Arul Antony (✉)
PG and Research Department of Chemistry,
Presidency College (Autonomous),
Chennai 60005, India
e-mail: mkavath15@gmail.com
e-mail: antonypresidency15@gmail.com

M. Durka
Department of Physics, A.V.V.M Sri
Pushpam College (Autonomous),
Poondi, Tamil Nadu 613503, India

($M_s = 80$ emu/g) at room temperature [6–8]. However, different values of H_c and M_s have been reported [9, 10] for nanosized $CoFe_2O_4$ particles, due to the fact that the magnetic property may depend on the particle size and preparation methods. The value of M_s in Mn^{2+}-doped $CoFe_2O_4$ is expected to depend on the cation distribution of the magnetic Fe^{3+}, Mn^{2+}, and Co^{2+} ions among the A– and B– sites [11, 12].

Several methods such as hydrothermal [13, 14], co-precipitation [15], thermal decomposition [16], sol-gel [17], and ball milling [18] techniques are usually employed for the preparation of spinel ferrites. The above methods have some disadvantages, such as a synthesis time duration that is too long, energy consumption, and the need for a very high temperature calcination step, and hence, further development of these methods is restricted to a certain extent. Moreover, Mn^{2+} doped $CoFe_2O_4$ is quite unstable in air, and Mn^{2+} ions on the surface oxidize to form Mn^{3+} ions, resulting in the dissociation of the ferrites at elevated temperatures $(200 - 1000°C)$ [19]. Therefore, the above-said methods involving higher temperatures are not suitable for the preparation of Mn^{2+} doped $CoFe_2O_4$ nanostructures [8].

However, the urea-assisted autocombustion method is suitable for preparing Mn-Co ferrites with high values of M_s and excellent temperature-oriented magnetic properties. This method has gained much attention in recent years because, the as-prepared materials are pure, ultra fine, and relatively strain free with a narrow size distribution. Also, this method offers many advantages over the other mentioned methods, such as simplicity, high crystallinity, and its adequacy for the preparation of large quantities of products without the need for higher processing temperatures [9, 20].

The catalytic property of the nanocrystalline ferrites crucially depends on the distribution of cations among the A- and B- sites of the spinel structure. Yan et al. [6] have prepared various spinel ferrites ($CuFe_2O_4$, $NiFe_2O_4$ $CoFe_2O_4$ and $ZnFe_2O_4$) by a citrate assisted sol-gel method using ethylenediaminetetraacetic acid (EDTA) as a templating agent. The best performance was reported by using $CoFe_2O_4$, whereby the oxidation of benzyl alcohol (63 % yields) with 93 % selectivity in respect to benzaldehyde was achieved Ramankutty and Sugunan [7] have reported the ferrospinels of Ni, Co, and Cu by a room temperature co-precipitation route, and the results were cobalt ferrite is the most active catalyst at lower activation temperatures, while the copper ferrite is the most active one at higher activation temperatures and nickel ferrite is the least active.

Substitution of magnetic (Mn^{2+}, Ni^{2+}, etc.) and non-magnetic (Zn^{2+}, Cd^{2+}, etc.) cations in spinel ferrites changes their optical, magnetic, and catalytic properties [21], due to the distribution of the cations in between the available A– and B– sites [22]. Several cations have been used as substituent by many researchers in order to improve the electrical and magnetic properties of spinel ferrites [23–25]. However, a detailed study on the optical and catalytic properties of Mn^{2+}-doped $CoFe_2O_4$ nanoparticles has not yet been reported so far.

In this aspect, the present investigation attempts to study the effects of Mn doping on the structural, morphological, optical, magnetic, and catalytic properties of $CoFe_2O_4$ ($Mn_xCo_{1-x}Fe_2O_4$; $x = 0.0, 0.1, 0.2, 0.3, 0.4$, and 0.5) nanoferrites by the urea-assisted autocombustion method. The as-prepared samples were characterized by using X-ray diffraction (XRD) followed by Rietveld refinements, high-resolution scanning electron microscopy (HR-SEM), high-resolution transmission electron microscopy (HR-TEM), energy-dispersive X-ray spectroscopy (EDX), UV-visible diffuse reflectance spectra (DRS), photoluminescence (PL) spectra, and vibrating sample magnetometer (VSM) techniques, and the obtained results were discussed. The product formed by the catalytic oxidation of benzyl alcohol was characterized by gas chromatography (GC). Benzyl alcohol oxidation activity test was carried out and reported the influence of the dopant (Mn^{2+}) on the catalytic activity of the $CoFe_2O_4$ spinel. The best activity and selectivity towards catalytic oxidation of benzyl alcohol were observed.

2 Experimental Part

2.1 Materials and Methods

All the chemicals used in this study were of analytical grade obtained from Merck, India, and were used as received without further purification. Cobalt nitrate ($Co(NO_3)_2 \cdot 6H_2O$, 98 %), manganese nitrate ($Mn(NO_3)_2 \cdot 4H_2O$, 98 %), ferric nitrate ($Fe(NO_3)_3 \cdot 9H_2O$, 98 %), and urea ($CO(NH_2)_2$) as the fuel are used for this autocombustion method. The samples were prepared with the addition of Mn^{2+} of different molar ratios ($Mn_xCo_{1-x}Fe_2O_4$; $x = 0.0, 0.1, 0.2, 0.3, 0.4$, and 0.5) to $CoFe_2O_4$. In the case of $CoFe_2O_4$, the reaction mixture was taken in the silica crucible, treated in an air furnace at 400°C for 2 h at a heating rate of 5 °C/min, and cooled at the same rate, and it became solid. Initially, the mixture was subjected to boiling and underwent evaporation followed by decomposition with the evolution of gases. When the solution reached the point of spontaneous combustion, it vaporized and instantly became a solid. After the completion of combustion reaction, the solid

powder was obtained and then it was washed well with ethanol and dried at 80°C for 30 min. The as-prepared samples ($Mn_xCo_{1-x}Fe_2O_4$ with x = 0.0, 0.1, 0.2, 0.3, 0.4, and 0.5) were labeled as $CoFe_2O_4$, $Mn_{0.1}Co_{0.9}Fe_2O_4$, $Mn_{0.2}Co_{0.8}Fe_2O_4$, $Mn_{0.3}Co_{0.7}Fe_2O_4$, $Mn_{0.4}Co_{0.6}Fe_2O_4$, and $Mn_{0.5}Co_{0.5}Fe_2O_4$, respectively.

The expected urea-assisted autocombustion reaction may be as follows: $Co(NO_3)_2 \cdot 6H_2O_{(s)} + 2Fe(NO_3)_3 \cdot 9H_2O_{(s)} + 6.66CO(NH_2)_{2(s)} \rightarrow CoFe_2O_{4(s)} + 37.33H_2O_{(g)} \uparrow + 6.66CO_{2(g)} \uparrow + 10.66N_{2(g)} \uparrow$

2.2 Characterization Techniques

Structural characterization of $Mn_xCo_{1-x}Fe_2O_4$ (x = 0.0, 0.1, 0.2, 0.3, 0.4, and 0.5) samples was performed using a Rigaku Ultima IV high-resolution X-ray diffractometer (XRD) with CuKα radiation at λ=1.5418 Å. Structural refinements using the Rietveld method were carried out using the PDXL program, and both refined lattice parameter and crystallite size of the obtained ferrites are reported. Morphological studies and energy-dispersive X-ray analysis have been performed with a JEOL JSM6360 HR-SEM equipped with EDX for elemental chemical analysis. The transmission electron micrographs were carried out by Philips TEM (CM20). The surface area was derived from the N_2 adsorption-desorption isotherms using liquid nitrogen at 77 K using an automatic adsorption instrument (Quantachrome Corp. Nova-1000 gas sorption analyzer). UV-visible DRS was recorded using a Cary 100 UV-visible spectrophotometer to estimate their bandgap energy (E_g). The PL properties were recorded using Varian Cary Eclipse Fluorescence Spectrophotometer. Magnetic measurements were carried out at room temperature using a PMC MicroMag 3900 model VSM equipped with a 1-T magnet.

2.3 Catalytic Test

The oxidation of benzyl alcohol into benzaldehyde using spinel $Mn_xCo_{1-x}Fe_2O_4$ (x = 0.0, 0.1, 0.2, 0.3, 0.4, and 0.5) catalysts were carried out in a batch reactor operated under atmospheric conditions. Ten millimoles of an oxidant (H_2O_2) was added along with 1 g of nanosized catalysts ($CoFe_2O_4$, $Mn_{0.1}Co_{0.9}Fe_2O_4$, $Mn_{0.2}Co_{0.8}Fe_2O_4$, $Mn_{0.3}Co_{0.7}Fe_2O_4$, $Mn_{0.4}Co_{0.6}Fe_2O_4$, and $Mn_{0.5}Co_{0.5}Fe_2O_4$), and the contents were heated at 80°C in an acetonitrile medium for 10 h in a three-necked round bottom flask equipped with a reflux condenser and thermometer. The oxidized products after the catalytic reaction are collected and studied using an Agilent GC spectrometer. The column used for the study was a DB wax column (capillary column) of length 30 mm, and helium was used as the carrier gas.

## 3 Results and Discussion

3.1 Structural Analysis

The structure and phase purity of the samples were confirmed by analyzing the XRD patterns. Figure 1 shows the XRD patterns of $Mn_xCo_{1-x}Fe_2O_4$ samples prepared at various Mn^{2+} substitutions (x = 0.0, 0.1, 0.2, 0.3, 0.4, and 0.5). The main spinel diffraction peaks (2θ) appear at about 29.65°, 35.71°, 37.02°, 42.51°, 53.05°, 56.54°, 62.05°, 70.52°, 74.02°, and 79.03°, which are attributed to the (220), (311), (222), (400), (422), (511), (440), (620), (533), and (444) planes, respectively, and show the characteristics of a single-phase cubic spinel structure with an $Fd3m$ space group [17]. The XRD patterns are indexed using the JCPDS card no. 22-1086 for pure $CoFe_2O_4$ and Mn^{2+}-doped $CoFe_2O_4$. The XRD peaks indicate a well-defined spinel phase that was developed during the combustion. However, some peaks of the α-Fe_2O_3 phase can also be observed at 2θ = 33.08°, 41.02°, and 54.11° in each diffraction pattern. The formation of a small fraction of the α-Fe_2O_3 phase was mainly due to the partial oxidation of spinel $CoFe_2O_4$ and Mn-Co ferrites [25]. During the combustion process, conventional oxidation and formation of spinel $CoFe_2O_4$ and Co-Mn ferrite are very common. Besides, control of the furnace environment during complete combustion is also very crucial. The intensity of the main diffraction peak of the cubic spinel ferrite at the (311) plane was considered as a measure of its degree of crystallinity.

The average crystallite size of the spinel $Mn_xCo_{1-x}Fe_2O_4$ (x= 0.0, 0.1, 0.2, 0.3, 0.4, and 0.5) samples was calculated by using the Debye-Scherrer formula:

$$L = \frac{0.89\lambda}{\beta \cos\theta}$$

where L is the average crystallite size; λ, the X-ray wavelength; θ, the Bragg diffraction angle; and β, the full width at half maximum (FWHM). The estimated results showed that the average crystallite size was higher (36.45 nm) for pure $CoFe_2O_4$ However, when the Mn^{2+} doping concentrations (x = 0.1 to 0.5) were further increased a decrease in the crystallite size from 32.34 to 22.62 nm was observed. The calculated crystallite size is in good agreement with the results obtained by the Rietveld analysis.

**Fig. 1** XRD patterns of the $Mn_xCo_{1-x}Fe_2O_4$ ($x = 0.0$, 0.1, 0.2, 0.3, 0.4, and 0.5) samples
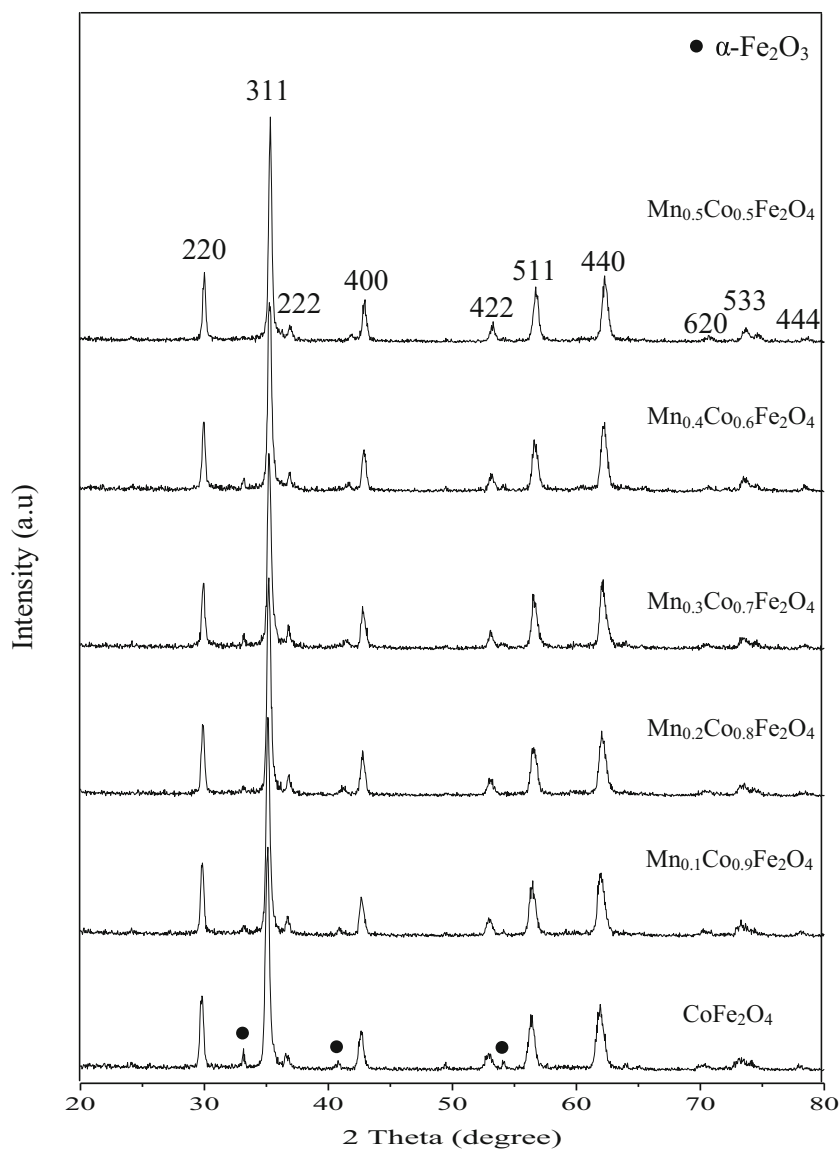
Rietveld analyses have been used to characterize the $Mn_xCo_{1-x}Fe_2O_4$ spinels in order to understand their physical properties (lattice parameter, crystallite size, and strain). Rietveld refinement XRD data analyses for the samples are shown in Fig. 2. In this, the calculated patterns are shown in the same field as a solid line curve. The difference observed minus calculated is shown in the lower field. During the Rietveld refinements, the goodness of fit is defined by the reliability factor $S = R_{wp}/R_e$, where R_{wp} and R_e are, respectively, the R-weighted and the R-expected patterns. The obtained values of the lattice parameter and crystallite size from the Rietveld refinement XRD analysis are shown in Fig. 3 (Table 1). The obtained lattice parameter value of pure $CoFe_2O_4$ is $a = 8.432$Å. However, in the present study, the value of the lattice parameter is increased from 8.437 to 8.457 Å with increasing of the

Mn^{2+} content ($x = 0.1$ to 0.5). The values of the lattice parameter exhibit an almost linear dependence, thus obeying Vegard's law [26] as shown in Fig. 3. The slight increasing trend in the lattice parameter is due to the replacement of the smaller ionic radius of Co^{2+}(0.72Å) [9, 27] by the larger ionic radius of Mn^{2+}(0.92Å) [13] in the host system. Zhuang et al. [13] reported that the lattice parameter decreases with increasing of the doping concentration of Zn^{2+} with a smaller ionic radius in $MnFe_2O_4$ nanoparticles.

3.2 Scanning Electron Microscopy Studies

Morphologies of the $Mn_xCo_{1-x}Fe_2O_4$ samples were recorded using a high-resolution scanning electron microscope (HR-SEM), and the images are shown in Fig. 4.

Fig. 2 XRD pattern refinements using the Rietveld method of the $Mn_xCo_{1-x}Fe_2O_4$ ($x = 0.0, 0.1, 0.2, 0.3, 0.4,$ and 0.5) samples (experimental data: *upper solid line* represents calculated pattern, and *lower solid line*, intensity difference)
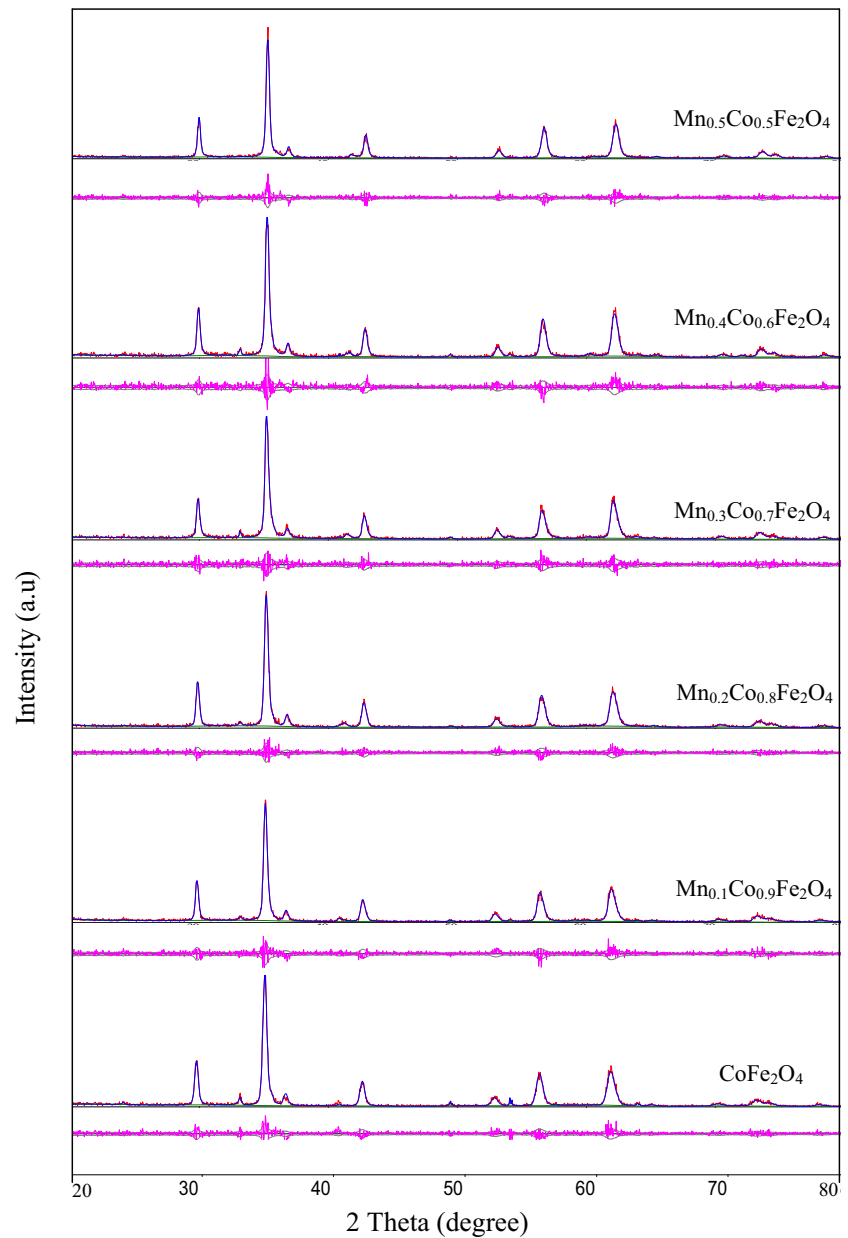
HR-SEM images indicated that the samples consist of nanosized particles, which are agglomerated together. All the particles had a well-crystallized surface morphology and an average grain size which is smaller than 100 nm. It clearly showed that the pure and Mn^{2+}-doped $CoFe_2O_4$ nanoparticles are agglomerated due to the presence of magnetic interactions among them. The crystallite size of the samples obtained from XRD is fairly consistent with the particle size determined by HR-SEM. The difference in shape and the average grain dimensions is correlated with the crystallite dimensions and ionic radii of the starting materials.

3.3 Transmission Electron Microscopy Analysis

To provide a further evidence for the formation and morphology of the as-synthesized Mn^{2+}-doped $CoFe_2O_4$ nanoparticles, high-resolution transmission electron microscopy (HR-TEM) analysis was carried out, and the image is shown in Fig. 5a. It is evident that the nanoparticles are uniform in size, which is consistent with the average size obtained from the peak broadening in X-ray diffraction (XRD) analysis and Rietveld refinement XRD analysis. The average size of the as-synthesized nanoparticles was found to be in the range of 25–38 nm. HR-TEM
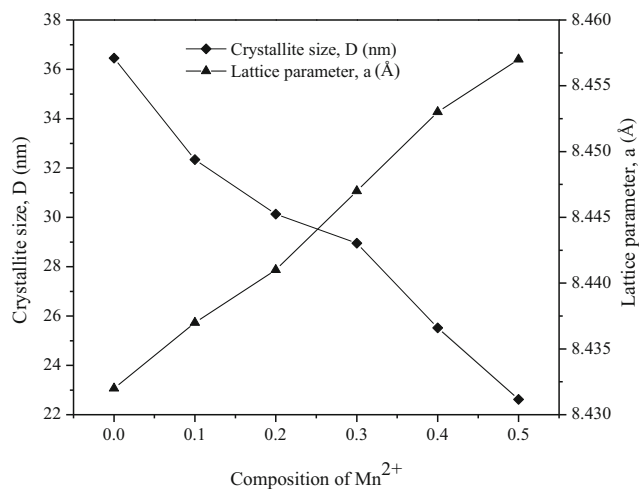
Fig. 3 Evolution of the lattice parameter and crystallite size of the $Mn_xCo_{1-x}Fe_2O_4$ ($x = 0.0, 0.1, 0.2, 0.3, 0.4,$ and 0.5) samples

micrographs clearly showed the nanoparticles with agglomeration due to the presence of the magnetic interactions among the particles. Selected area electron diffraction (SAED) pattern of Mn-doped $CoFe_2O_4$ nanoparticles is shown in Fig. 5b, which implies that the as-prepared samples are single crystalline in nature.

3.4 Energy-Dispersive X-Ray Analysis

Energy-dispersive X-ray (EDX) analysis of the $Mn_xCo_{1-x}Fe_2O_4$ samples is shown in Fig. 6. Figure 6a shows the peaks of Fe, Co, and O elements in pure $CoFe_2O_4$, and Fig. 6b shows the peaks of Fe, Mn, Co, and O elements for Mn-doped $CoFe_2O_4$ samples. The percentage of Co/Mn values obtained is given in the inset of Fig. 6a, b.

Mn-doped $CoFe_2O_4$ did not deviate from their initial stoichiometry and matched well with the initial degree of Mn^{2+} substitutions. It is interesting to note that the urea-assisted autocombustion method completely favors the formation of $CoFe_2O_4$. A small peak appeared at 2.1 keV for all the samples, which indicated the presence of a Au (gold) peak that has been used as a sputter coating while preparing the sample for HR-SEM analysis for a better visibility of the surface morphology.

3.5 N_2 Adsorption-Desorption Isotherms

The N_2 adsorption-desorption isotherm values of the $Mn_xCo_{1-x}Fe_2O_4$ ($x = 0.0, 0.1, 0.2, 0.3, 0.4,$ and 0.5) samples are given in Table 2. The spinel $CoFe_2O_4$ sample possessed a surface area of 38.42 m^2/g, whereas it was increased considerably to 68.96 m^2/g for $Mn_{0.5}Co_{0.5}Fe_2O_4$. The pore volume of $CoFe_2O_4$ is 0.192 cm^3/g and it is decreased with increasing the BET surface area, and the sample $Mn_{0.5}Co_{0.5}Fe_2O_4$ possessed 0.129 cm^3/g. Similarly, the average pore diameter of $Mn_{0.5}Co_{0.5}Fe_2O_4$ was increased to 97.33 Å, but it was only 91.32 Å for pure $CoFe_2O_4$ (Fig. 7).

The surface area of $Mn_{0.5}Co_{0.5}Fe_2O_4$ (68.96 m^2/g) was found to be higher than that of pure $CoFe_2O_4$ (38.42 m^2/g), and it is due to the smaller particle size of the $Mn_{0.5}Co_{0.5}Fe_2O_4$ than $CoFe_2O_4$, which is also confirmed by HR-SEM and XRD results. Therefore, it is believed that the high surface area of $Mn_{0.5}Co_{0.5}Fe_2O_4$ could enhance the catalytic properties than that of undoped $CoFe_2O_4$ sample.
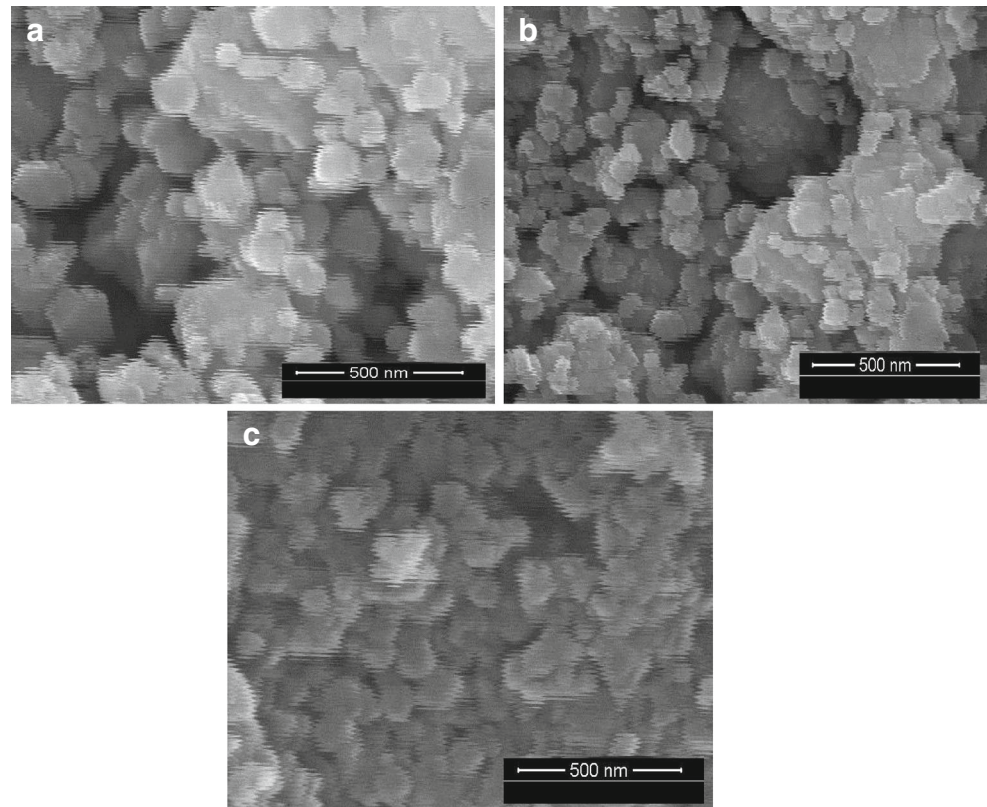
3.6 Diffuse Reflectance Spectroscopy

To give the significant information in relation to the effect of crystallite size on the optical properties of the

Table 1 Lattice parameter and crystallite size (Scherrer formula, Rietveld analysis) of the $Mn_xCo_{1-x}Fe_2O_4$ ($x = 0.0, 0.1, 0.2, 0.3, 0.4,$ and 0.5) samples

Samples	Lattice parameter (Å)	Crystallite size, L (nm)		Band gap (eV)	Strain (%)	S (goodness of fit)
	(Rietveld analysis)	Scherrer formula	Rietveld analysis			
$CoFe_2O_4$	8.432	36.45	38	2.33	0.452	1.14
$Mn_{0.1}Co_{0.9}Fe_2O_4$	8.437	32.34	35	2.35	0.441	1.12
$Mn_{0.2}Co_{0.8}Fe_2O_4$	8.441	30.13	31	2.37	0.433	1.11
$Mn_{0.3}Co_{0.7}Fe_2O_4$	8.447	28.95	28	2.38	0.411	1.07
$Mn_{0.4}Co_{0.6}Fe_2O_4$	8.453	25.52	24	2.40	0.362	1.09
$Mn_{0.5}Co_{0.5}Fe_2O_4$	8.457	22.62	21	2.42	0.355	1.13

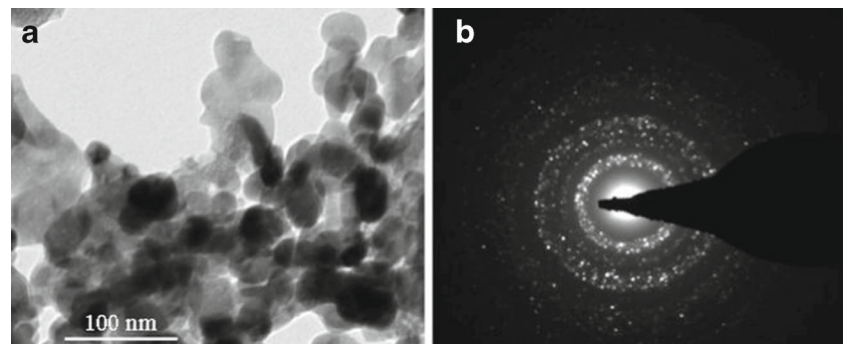**Fig. 4** HR-SEM images of **a** pure $CoFe_2O_4$, **b** $Mn_{0.3}Co_{0.7}Fe_2O_4$, and **c** $Mn_{0.5}Co_{0.5}Fe_2O_4$ samples

$Mn_xCo_{1-x}Fe_2O_4$ ($x = 0.0, 0.1, 0.2, 0.3, 0.4,$ and 0.5) samples, UV-visible diffuse reflectance spectroscopy (DRS) studies were carried out at room temperature The bandgap energy (E_g) of the samples can be evaluated using the Kubelka-Munk model. It allows the calculation of the absorption coefficient (α) by the measurement of UV-visible diffuse reflectance, and it is mainly used for powder samples. All the samples display optical properties at the visible region, which is due to the bandgap transition of the $Mn_xCo_{1-x}Fe_2O_4$ samples and it is in agreement with the black color of the samples. The Kubelka-Munk function,
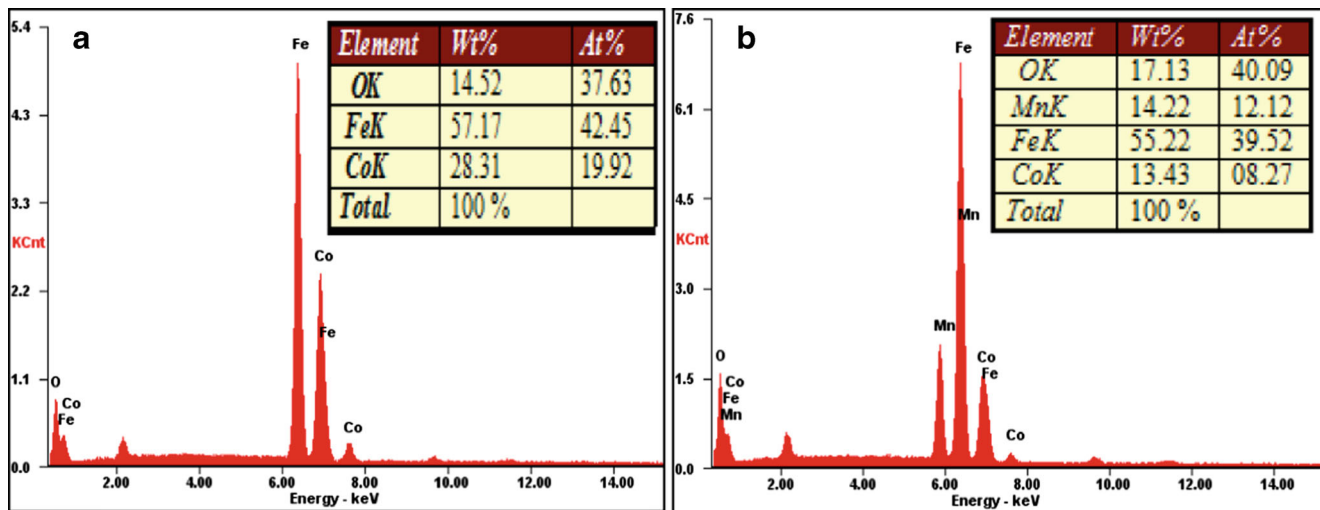
$F(R)$, is directly proportional to the absorption coefficient (α), and the value is estimated from the following equation:

$$(F(R)) = \alpha = \frac{(1-R)^2}{2R}$$

where $F(R)$ is the Kubelka-Munk function; α, the absorbance; and R, the reflectance. A graph is plotted between $[F(R)h\upsilon]^2$ and $h\upsilon$; the intercept value is the bandgap energy and these are shown in Fig. 8a–f. The estimated bandgap values of the $Mn_xCo_{1-x}Fe_2O_4$ ($x = 0.0, 0.1, 0.2, 0.3, 0.8,$ and 0.5) nanoparticles are 2.33, 2.35, 2.37,

Fig. 5 HR-TEM image (**a**) and SAED patterns (**b**) of the $Mn_{0.5}Co_{0.5}Fe_2O_4$ samples

a

Element	Wt%	At%
OK	14.52	37.63
FeK	57.17	42.45
CoK	28.31	19.92
Total	100 %	

b

Element	Wt%	At%
OK	17.13	40.09
MnK	14.22	12.12
FeK	55.22	39.52
CoK	13.43	08.27
Total	100 %	

Fig. 6 EDX spectra of **a** pure $CoFe_2O_4$ and **b** $Mn_{0.5}Co_{0.5}Fe_2O_4$ samples

2.38, 2.40, and 2.42 eV, respectively (Fig. 9 and Table 1). It is inferred that there is an increase in the bandgap of doped samples when compared to the pure $CoFe_2O_4$. The bandgap (E_g) value of pure $CoFe_2O_4$ is 2.33 eV, and hence, there is a blue shift for all Mn-doped $CoFe_2O_4$ samples. A similar value (2.38 eV) was reported previously by Chen et al. [17] for pure $CoFe_2O_4$. The significant feature in this case is a direct relationship between the grain size of the nanoparticles and optical bandgap energy. A small increase in the optical bandgap energy with decreasing of the crystallite size indicates a very weak quantum size effect [28, 29]. This result is in good agreement with the Rietveld analysis, which suggested that the crystallite size of the samples slightly decreases with increasing Mn^{2+} content.

3.7 Photoluminescence Spectroscopy

Photoluminescence (PL) spectroscopy was recorded at room temperature to investigate the recombination phenomena of the semiconductor materials. Also, PL spectroscopy gives information on the bandgap with the relative energetic position of sub-bandgap defect states and nanometer size effect of the particles may reflect its optical property. Figure 10 shows the room temperature PL spectra of the $Mn_xCo_{1-x}Fe_2O_4$ ($x = 0.0, 0.1, 0.2, 0.3, 0.4,$ and 0.5) samples recorded at the excitation wavelength of 235 nm. Two main PL peaks were observed at wavelengths of around 530 and 758 nm corresponding to 2.33 and 1.63 eV, respectively. The higher energy peak was attributed to the bandgap of $CoFe_2O_4$ nanoparticles, i.e., 2.33 eV. Similar results were reported earlier by Chen et al. [17] and they observed two main PL peaks at wavelengths of 520 and 760 nm corresponding to the bandgap energy of 2.38 and 1.63 eV, respectively. The peaks at 422 and 453 nm correspond to the violet emission due to the radiative defects related to the interface traps existing at the grain boundaries [30, 31]. The main peak at 530 nm may be attributed to the oxygen vacancies giving rise to green emissions [32]. Yellow emissions are observed by the appearance of peaks at 570 and 595 nm, which are attributed to the interstitial oxygen defects. In the deep-level emission, all samples display a defect-related visible luminescence band; this is usually related to defects such as interstitial defect and oxygen vacancies [33].

Table 2 BET surface area, average pore diameter, and pore volume of the $Mn_xCo_{1-x}Fe_2O_4$ ($x = 0.0, 0.1, 0.2, 0.3, 0.4,$ and 0.5) samples

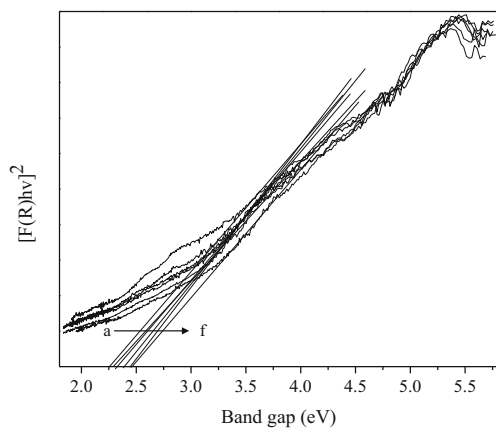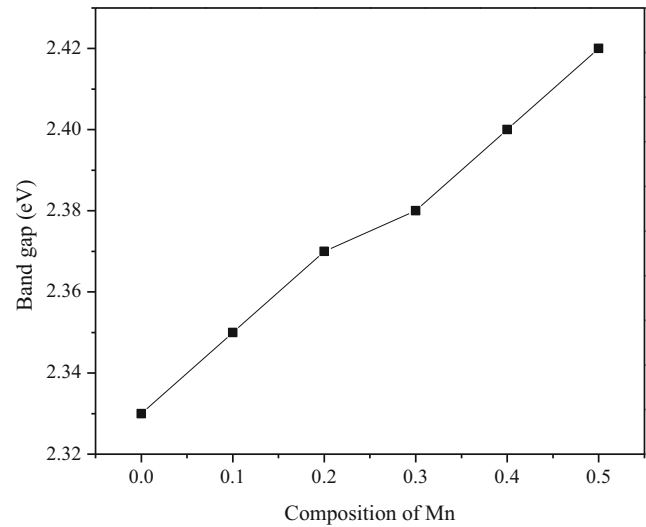| Samples	BET surface area (m^2/g)	Average pore diameter (Å)	Pore volume (cm^3/g)
$CoFe_2O_4$	38.42	91.32	0.192
$Mn_{0.1}Co_{0.9}Fe_2O_4$	40.31	93.65	0.176
$Mn_{0.2}Co_{0.8}Fe_2O_4$	47.53	95.71	0.169
$Mn_{0.3}Co_{0.7}Fe_2O_4$	52.67	96.92	0.158
$Mn_{0.4}Co_{0.6}Fe_2O_4$	59.74	97.58	0.145
$Mn_{0.5}Co_{0.5}Fe_2O_4$	68.96	98.53	0.129
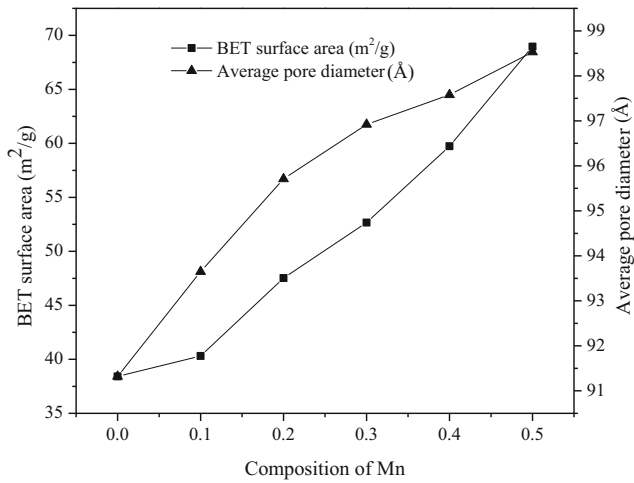
Fig. 7 BET surface area and average pore diameter of the $Mn_xCo_{1-x}Fe_2O_4$ ($x = 0.0, 0.1, 0.2, 0.3, 0.4,$ and 0.5) samples

Fig. 9 Variation of the bandgap energy of the spinel $Mn_xCo_{1-x}Fe_2O_4$ ($x = 0.0, 0.1, 0.2, 0.3, 0.4,$ and 0.5) samples

The decrease in the green emission (530 nm) intensity with increasing of the Mn^{2+} content, and decrease of crystallite size suggest the presence of various structural defects [34] and the expansion of the bandgap, E_g. It may be due to the decreasing number of optically active defects as well as the thermal quenching because of the increase in the non-radiative transition centers created by Mn^{2+} incorporation and intrinsic defects [35–37]. It is believed that the expansion of the bandgap, E_g, is related to the charge transfer transition between the donor and/or acceptor ionization levels of Mn^{2+} ions [38]. The addition of Mn^{2+} in $CoFe_2O_4$ reduces the particle size, which can be confirmed by the blue shift in the PL spectra. The maximum emission is shifted to lower energies as the particle size was decreased, which might be related to the quantum confinement effect.
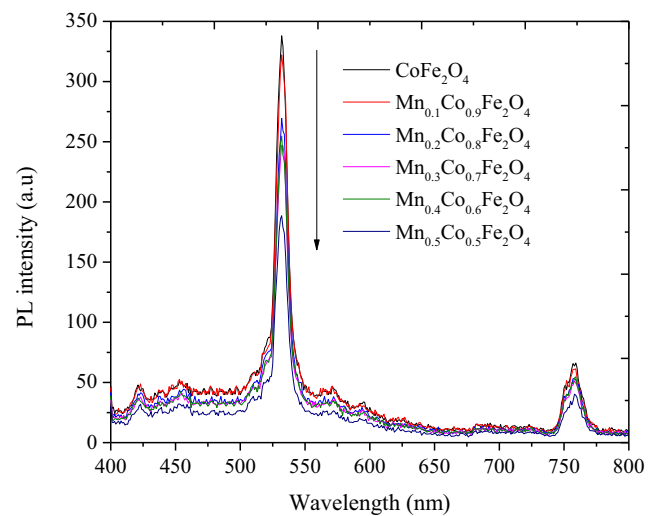
3.8 VSM Measurements

Magnetic properties of the nanosized ferrites depend on composition as well as distribution of cations in tetrahedral (A–) and octahedral (B–) sites. According to the occupancy of the cations in the A– and B– sites, they can exhibit ferromagnetic, anti-ferromagnetic, and paramagnetic nature [39–41]. Mainly, the chemical composition and the particle size play a vital role in determining the magnetic property of the spinel ferrites. In this present study, the magnetic properties of the $Mn_xCo_{1-x}Fe_2O_4$ ($x = 0.0, 0.1, 0.2, 0.3, 0.4,$ and 0.5) samples were recorded at room temperature using a

Fig. 8 UV-visible diffuse reflectance spectra of the **a** $CoFe_2O_4$, **b** $Mn_{0.1}Co_{0.9}Fe_2O_4$, **c** $Mn_{0.2}Co_{0.8}Fe_2O_4$, **d** $Mn_{0.3}Co_{0.7}Fe_2O_4$, **e** $Mn_{0.4}Co_{0.6}Fe_2O_4$, and **f** $Mn_{0.5}Co_{0.5}Fe_2O_4$ samples

Fig. 10 PL spectra of the $Mn_xCo_{1-x}Fe_2O_4$ ($x = 0.0, 0.1, 0.2, 0.3, 0.4,$ and 0.5) samples

Fig. 11 Magnetic hysteresis (M-H) loops of the $Mn_xCo_{1-x}Fe_2O_4$ ($x = 0.0, 0.1, 0.2, 0.3, 0.4,$ and 0.5) samples
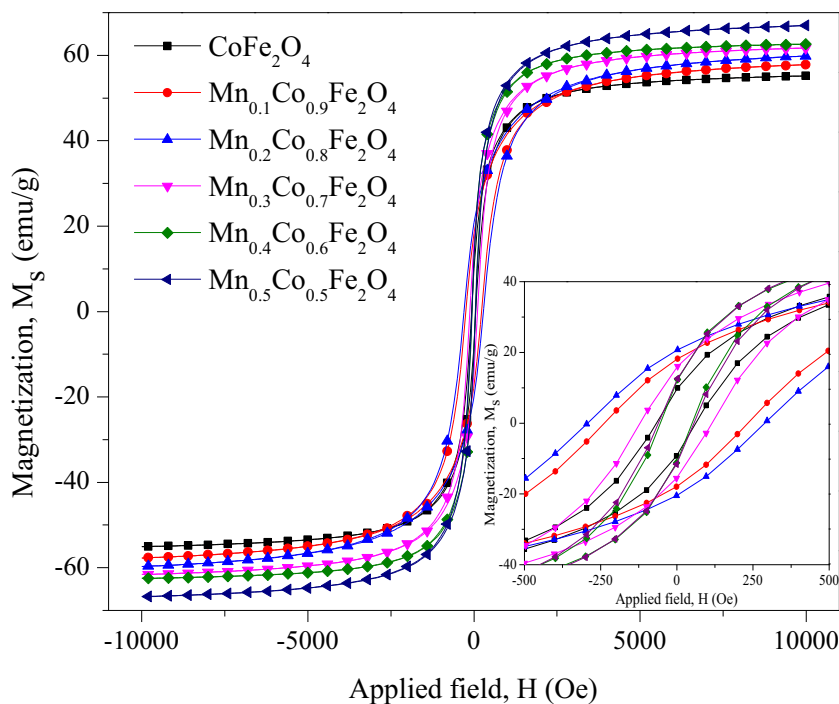
vibrating sample magnetometer (VSM) in the applied field range from -10 to $+10$ kOe. Figure 11 shows a typical magnetic hysteresis loop of the $Mn_xCo_{1-x}Fe_2O_4$ samples, indicating the presence of ordered magnetic domains of the spinel ferrites [42]. The sample $CoFe_2O_4$ shows the superparamagnetic behavior where magnetization increases with the applied field and does not saturate even at 10 kOe. The observed saturation magnetization (M_s), remanent magnetization (M_r), and coercivity (H_c) values are reported in Table 3. The prepared lower composition ($x = 0.0$, i.e. pure $CoFe_2O_4$) shows a superparamagnetic behavior, and the higher compositions ($x = 0.1, 0.2, 0.3, 0.4,$ and 0.5) show a weak ferromagnetic behavior with hysteresis and that the M_s increased with increasing Mn content to reach a maximum value of 66.92 ± 05 emu/g for $Mn_{0.5}Co_{0.5}Fe_2O_4$.

However, it was observed that the H_c and M_r values of the spinel $Mn_xCo_{1-x}Fe_2O_4$ nanoparticles gradually increased with the increase of Mn^{2+} content until $x = 0.2$, and rapidly decreased for x larger than 0.2, i.e. $x = 0.3$, 0.4 and 0.5 (Table 3); this can be attributed to the magnetic character and the anisotropic nature of cobalt substituted by manganese. The obtained result shows that the value of M_s is lower (55.16 ± 24 emu/g) for pure $CoFe_2O_4$, and it is increased from 57.75 ± 31 to 66.92 ± 05 emu/g with increase of the concentration of Mn^{2+} ($x = 0.1$ to 0.5), which can be attributed to the smaller magnetic moments of Co^{2+} ions (3 μB) substituted by the higher magnetic moments of Mn^{2+} ions (5 μB) at the octahedral sites [43–45]. From the M-H loop, it can be observed that the spinel $Mn_{0.5}Co_{0.5}Fe_2O_4$ nanoparticles show high saturation magnetization (M_s) justified by the high anisotropy

Table 3 Variation of coercivity (H_c), remanent magnetization (M_r), and saturation magnetization (M_s) of the $Mn_xCo_{1-x}Fe_2O_4$ ($x = 0.0, 0.1, 0.2, 0.3, 0.4,$ and 0.5) samples

| Samples	H_c (Oe)	M_r (emu/g)	M_s (emu/g)
$CoFe_2O_4$	69.52 ± 05	09.75 ± 02	55.16 ± 24
$Mn_{0.1}Co_{0.9}Fe_2O_4$	240.11 ± 13	18.12 ± 07	57.75 ± 31
$Mn_{0.2}Co_{0.8}Fe_2O_4$	296.97 ± 47	20.63 ± 11	58.89 ± 18
$Mn_{0.3}Co_{0.7}Fe_2O_4$	122.16 ± 36	15.72 ± 06	61.53 ± 21
$Mn_{0.4}Co_{0.6}Fe_2O_4$	62.41 ± 15	12.68 ± 12	62.68 ± 08
$Mn_{0.5}Co_{0.5}Fe_2O_4$	55.53 ± 42	11.93 ± 24	66.92 ± 05

and small dimensions of the grains. The M_s value of pure $CoFe_2O_4$ is 55.16 ± 24 emu/g, which is lower than that of the earlier reported values, i.e., 59.0 emu/g [8] and 93.9 emu/g (bulk) [46]. The observed difference in the value of M_s might be due to particle size, crystalline nature and arrangement of the particles, as well as the nature and composition of the dopant. The values obtained in our study can be explained by the preparation method and the size of grains [47, 48].

3.9 Catalytic Oxidation of Benzyl Alcohol

The catalytic oxidation of benzyl alcohol was studied by using pure and Mn^{2+}-doped $CoFe_2O_4$ nanocatalysts to investigate their performance as catalysts. One gram of prepared ferrite nanocatalyst ($CoFe_2O_4$, $Mn_{0.1}Co_{0.9}Fe_2O_4$, $Mn_{0.2}Co_{0.8}Fe_2O_4$, $Mn_{0.3}Co_{0.7}Fe_2O_4$, $Mn_{0.4}Co_{0.6}Fe_2O_4$, and $Mn_{0.5}Co_{0.5}Fe_2O_4$) along with the oxidant H_2O_2 (10 mmol) in an acetonitrile medium was placed in a batch reactor. The conversion of benzyl alcohol into benzaldehyde reached a maximum of 92.62 % for $Mn_{0.5}Co_{0.5}Fe_2O_4$, whereas for $CoFe_2O_4$, the conversion was only 62.75 % with 100 % selectivity (Table 4 and Fig. 12). However, in our present work, the sample $Mn_{0.5}Co_{0.5}Fe_2O_4$ performs as a good catalyst with higher yield of benzaldehyde with good selectivity than other samples. Hence, the dopant metal (Mn^{2+}) ion is important, which in turn is active for the catalytic oxidation reaction. Moreover, a heterogeneous catalyst like the Mn-doped $CoFe_2O_4$ spinel is non-toxic and environmentally friendly and has excellent catalytic performance. The best performance was achieved on the spinel $CoFe_2O_4$, whereby 93 % selectivity of benzaldehyde at 63 % conversion of benzyl alcohol was shown by Yan et al. [6]. It is reported earlier that the cobalt ferrite is the most active catalyst at a lower activation temperature [7]. However, in our present study, the sample $Mn_{0.5}Co_{0.5}Fe_2O_4$ acts as a good catalyst with higher yield of benzaldehyde with good selectivity as compared to the other ($CoFe_2O_4$, $Mn_{0.1}Co_{0.9}Fe_2O_4$, $Mn_{0.2}Co_{0.8}Fe_2O_4$, $Mn_{0.3}Co_{0.7}Fe_2O_4$, and $Mn_{0.4}Co_{0.6}Fe_2O_4$) samples.

Table 4 The conversion and selectivity of catalytic oxidation of benzyl alcohol into benzaldehyde

Catalyst	Conversion (%)	Selectivity (%)
$CoFe_2O_4$	62.75	100
$Mn_{0.1}Co_{0.9}Fe_2O_4$	65.60	100
$Mn_{0.2}Co_{0.8}Fe_2O_4$	75.61	100
$Mn_{0.3}Co_{0.7}Fe_2O_4$	82.98	100
$Mn_{0.4}Co_{0.6}Fe_2O_4$	87.54	100
$Mn_{0.5}Co_{0.5}Fe_2O_4$	92.62	100
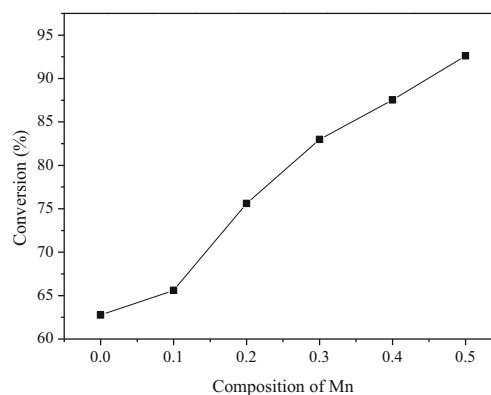
Fig. 12 Catalytic oxidation and conversion of the $Mn_xCo_{1-x}Fe_2O_4$ ($x = 0.0, 0.1, 0.2, 0.3, 0.4,$ and 0.5) samples

4 Conclusions

Nanosized $Mn_xCo_{1-x}Fe_2O_4$ ($x = 0.0, 0.1, 0.2, 0.3, 0.4,$ and 0.5) samples were successfully synthesized by the urea-assisted autocombustion method. The formation of the cubic spinel phase was confirmed by XRD and the Rietveld method. The average crystallite size of the samples was estimated using the Debye-Scherrer formula and was found to be in the range of 22.62 and 36.45 nm. Rietveld results showed the lattice parameter increased from 8.432 to 8.457 Å by increasing the Mn^{2+} content due to the larger ionic radius (0.92 Å) of Mn^{2+} ions than the smaller ionic radius of Co^{2+} (0.72 Å) ions. UV-visible diffuse reflectance spectroscopy (DRS) showed the bandgap energy (E_g) of the pure $CoFe_2O_4$ is 2.33 eV, and by increasing the Mn^{2+} ions, it increased from 2.35 to 2.42 eV. VSM measurements for the pure $CoFe_2O_4$ sample showed a superparamagnetic behavior, whereas the Mn^{2+}-doped $CoFe_2O_4$ ($x = 0.1, 0.2, 0.3, 0.4,$ and 0.5) samples showed a weak ferromagnetic behavior with hysteresis and that the M_s increased with increasing the Mn content to reach a maximum value of 66.92 ± 05 emu/g for $Mn_{0.5}Co_{0.5}Fe_2O_4$. Spinel $Mn_xCo_{1-x}Fe_2O_4$ nanostructures were used as catalysts for the conversion of benzyl alcohol with a conversion efficiency of 62.75 % for pure $CoFe_2O_4$ and 92.62 % for the $Mn_{0.5}Co_{0.5}Fe_2O_4$ spinel catalyst. The substitution of Mn^{2+} ions in $CoFe_2O_4$ plays a significant role in the alternation and development of the crystal structure, morphology, and optical, magnetic, and catalytic characteristics of the Co ferrite.

References

1. Song, Q., Zhang, Z.J.: J. Am. Chem. Soc. **126**, 6164 (2004)
2. Karaoglu, E., Baykal, A.: J. Supercond. Nov. Magn. **27**, 2041 (2014)
3. Amiri, S., Shokrollahi, H.: Mater. Sci. Eng. C **33**, 1 (2013)
4. Manikandan, A., Antony, S.A.: J. Supercond. Nov. Magn. **27**, 2725 (2014)
5. Koseoglu, Y., Baykal, A., Toprak, M.S., Gozuak, F., Basaran, A.C., Aktas, B.: J. Alloys Compd. **462**, 209 (2008)
6. Yan, K., Wu, X., An, X., Xie, X.: J. Alloys Compd. **552**, 405 (2013)
7. Ramankutty, C.G., Sugunan, S.: App. Catal. A: Gen. **218**, 39 (2001)
8. Koseoglu, Y., Alan, F., Tan, M., Yilgin, R., Ozturk, M.: Ceram. Int. **38**, 3625 (2012)
9. Koseoglu, Y., Baykal, A., Gozuak, F., Kavas, H.: Polyhedron **28**, 2887 (2009)
10. Kasapoglu, N., Baykal, A., Koseoglu, Y., Toprak, M.S.: Scripta Mater. **57**, 441 (2007)
11. Azam, A., Jawad, A., Ahmed, A.S., Chaman, M., Naqvi, A.H.: J. Alloys Compd. **509**, 2909 (2011)
12. Jawad, A., Ahmed, A.S., Ashraf, S.S.Z., Chaman, M., Azam, A.: J. Alloys Compd. **530**, 63 (2012)
13. Zhuang, L., Zhang, W., Zhao, Y., Li, D., Wu, W., Shen, H.: Powder Technol. **217**, 46 (2012)
14. Koseoglu, Y., Oleiwi, M.I.O., Yilgin, R., Kocbay, A.N.: Ceram. Int. **38**, 6671 (2012)
15. Akhtar, M.J., Younas, M.: Solid State Sci. **14**, 1536 (2012)
16. Gao, R.R., Zhang, Y., Yu, W., Xiong, R., Shi, J.: J. Magn. Magn. Mater. **324**, 2534 (2012)
17. Chen, J., Wang, Y., Deng, Y.: J. Alloys Compd. **552**, 65 (2013)
18. Aslibeiki, B., Kameli, P., Salamati, H., Eshraghi, M., Tahmasebi, T.: J. Magn. Magn. Mater. **322**, 2929 (2010)
19. Mostafa, N.Y., Zaki, Z.I., Heiba, Z.K.: J. Magn. Magn. Mater. **329**, 71 (2013)
20. Azam, A.: J. Alloys Compd. **540**, 145 (2012)
21. Arora, M., Chauhan, S., Sati, P.C., Kumar, M.: J. Supercond. Nov. Magn. **27**, 1867 (2014)
22. Khan, M.A., Islam, M.U., Ishaque, M., Rahman, I.Z.: J. Alloys Compd. **519**, 156 (2012)
23. Zhang, C.F., Zhong, X.C., Yu, H.Y., Liu, Z.W., Zeng, D.C.: Physica B **404**, 2327 (2009)
24. Shaikh, P.A., Kambale, R.C., Rao, A.V., Kolekar, Y.D.: J. Alloys Compd. **492**, 590 (2010)
25. Waqas, H., Qureshi, A.H., Subhan, K., Shahzad, M.: Ceram. Int. **38**, 1235 (2012)
26. Gabal, M.A., Allah, S.S.A.: Mater. Chem. Phys. **85**, 104 (2004)
27. Tahar, L.B., Basti, H., Herbst, F., Smiri, L.S., Quisefit, J.P., Yaacoub, N., Greneche, J.M., Ammar, S.: Mater. Res. Bull. **47**, 2590 (2012)
28. Kislova, N., Srinivasan, S.S., Emirov, Y., Stefanakos, E.K.: Mater. Sci. Eng. B **153**, 70 (2008)
29. Ng, C.H.B., Fan, W.Y.: J. Phys. Chem. B **110**, 20801 (2006)
30. Zang, C.H., Zhang, D.M., Tang, C.J., Fang, S.J., Zong, Z.J., Yang, Y.X., Zhao, C.H., Zhang, Y.S.: J. Phys. Chem. C **113**, 18527 (2009)
31. Zhuge, L.J., Wu, X.M., Wu, Z.F., Yang, X.M., Chen, X.M., Chen, Q.: Mater. Chem. Phys. **120**, 480 (2010)
32. Bhargava, R., Sharma, P.K., Dutta, R.K., Kumar, S., Pandey, A.C., Kumar, N.: Mater. Chem. Phys. **120**, 393 (2010)
33. Yilmaz, S., Bacaksiz, E., McGlynn, E., Polat, I., Ozcan, S.: Thin Solid Films **520**, 5172 (2012)
34. Lu, J.G., Chang, P., Fan, Z.: Mater. Sci. Eng. R **52**, 49 (2006)
35. Ozgur, U., Alivov, Y.I., Liu, C., Teke, A., Reshchikov, M.A., Dogan, S., Avrutin, V., Cho, S.J., Morkoc, H.: J. Appl. Phys. **98**, 041301 (2005)
36. Look, D.C., Farlow, G.C., Reunchan, P., Limpijumnong, S., Zhang, S.B., Nordlund, K.: Phys. Rev. Lett. **95**, 225502 (2005)
37. Shuang, D., Zhu, X.X., Wang, J.B., Zhong, X.L., Huang, G.J., He, C.: Appl. Surf. Sci. **257**, 6085 (2011)
38. Phan, T.L.: Solid State Commun. **151**, 24 (2011)
39. Mahmud, S.T., Hossain, A.A., Hakim, A.A., Seki, M., Kawai, T., Tabata, H.: J. Magn. Magn. Mater. **305**, 269 (2006)
40. Hankare, P.P., Pandav, R.S., Patil, R.P., Vader, V.T., Garadkar, K.M.: J. Alloys Compd. **544**, 197 (2012)
41. Hankare, P.P., Sanadi, K.R., Garadkar, K.M., Patil, D.R., Mulla, I.S.: J. Alloys Compd. **553**, 383 (2013)
42. Pazhanivelu, V., Selvadurai, A.P.B., Murugaraj, R.: J. Supercond. Nov. Magn. **27**, 1737 (2014)
43. Koseoglu, Y.: Ceram. Int. **39**, 4221 (2013)
44. Kambale, R.C., Shaikh, P.A., Harale, N.S., Bilur, V.A., Kolekar, Y.D., Bhosale, C.H., Rajpure, K.Y.: J. Alloys Compd. **490**, 568 (2010)
45. Yadav, S.P., Shinde, S.S., Kadam, A.A., Rajpure, K.Y.: J. Alloys Compd. **555**, 330 (2013)
46. Gherca, D., Pui, A., Cornei, N., Cojocariu, A., Nica, V., Caltun, O.: J. Magn. Magn. Mater. **324**, 3906 (2012)
47. Kurmude, D.V., Kale, C.M., Aghav, P.S., Shengule, D.R., Jadhav, K.M.: J. Supercond. Nov. Magn. **27**, 1889 (2014)
48. Kumar, L., Kumar, P., Srivastava, S.K., Kar, M.: J. Supercond. Nov. Magn. **27**, 1677 (2014)